



Impact of rheology on the resolution of linear kinematic features in the MITgcm

Eva Lemaire

Supervisor : Dr. Martin Losch

Alfred Wegener Institut, Bremerhaven, GERMANY

June 2024

Contents

1	Résumé stage	2
2	Internship summary	2
3	Institute Presentation	3
4	Abstract	3
5	Introduction	4
6	Method	5
6.1	RGPS	5
6.2	Simulations	5
6.2.1	Elliptical Yield Curve	7
6.2.2	Mohr-Coulomb with elliptical plastic potential (M.C.E.): .	8
6.2.3	Generalized Truncated Ellipse Method (T.E.M.) :	8
6.2.4	Teardrop	9
6.3	Detection Algorithm	10
6.3.1	Data Processing and Filtering	11
6.3.2	Segment Detection	11
6.3.3	Reconnection	11
6.4	Tracking Algorithm	12
7	Results	15
7.1	Number of LKFs	15
7.2	Length	16
7.2.1	Total length	16
7.2.2	LKF length	16
7.3	Intersection Angle	18

7.4	Lifetime	21
8	Outlook / Conclusion	22
9	Code availability	23

List of Figures

1	Schematic Yield Curves	7
2	Total deformation rate map	13
3	Number of LKFs	14
4	Total length of LKFs	17
5	LKF length	18
6	Schematic intersection angles	19
7	Intersection angles	20
8	Lifetime	22

List of Tables

1	Model parameters	9
2	Detection parameters	12

1 Résumé stage

Ce stage a été effectué dans le cadre de la complétion du M2 : Études des climats de la Terre. Il s'est déroulé au Alfred Wegener Institut à Bremerhaven en Allemagne dans l'équipe de dynamique du climat dirigée par le Prof. Dr. Thomas Jung. Le superviseur de ce stage est le Dr. Martin Losch, qui avec son équipe, travaille sur l'étude de la glace de mer et sa représentation dans le modèle de circulation générale développé par le Massachusetts Institute of Technology ; le MITgcm. Ce stage a porté sur l'étude de la résolution des Linear Kinematic Features (LKF) par le MITgcm en faisant varier les courbes d'état de contrainte dans le modèle. Pour cela, 7 simulations ont été réalisées. Une adaptation d'un algorithme de détection et de suivi des LKFs a été nécessaire afin d'obtenir des résultats comparables à la littérature. Une fois ces LKFs obtenus, une analyse statistique a été réalisée afin de les comparer aux LKFs détectés à partir de données d'observation. Ce stage a donc permis l'évaluation des performances du modèle MITgcm dans la résolution des LKFs pour différentes courbes d'état de contrainte.

2 Internship summary

This internship was carried out as part of the completion of the M2: Studying the Climates of the Earth. It took place at the Alfred Wegener Institute in

Bremerhaven, Germany, in the climate dynamics team headed by Prof. Dr. Thomas Jung. The supervisor was Dr. Martin Losch, who and his team are working on the study of sea ice and its representation in the Massachusetts Institute of Technology’s general circulation model, MITgcm. This internship focused on studying the resolution of Linear Kinematic Features (LKF) by the MITgcm, by varying the yield curves in the model. To this end, 7 simulations were carried out. An algorithm for detecting and tracking LKFs had to be adapted to obtain results comparable to the literature. Once these LKFs had been obtained, a statistical analysis was carried out to compare them with LKFs detected from observational data. This internship led to the evaluation of the MITgcm model’s performance in resolving LKFs for different yield curves.

3 Institute Presentation

This study has been conducted at the Alfred Wegener Institute. The Alfred Wegener Institute is a renowned scientific laboratory specializing in polar regions. It is located in Germany and has five main sites - Bremerhaven (where this study was conducted), Potsdam, Heligoland, Sylt, and Oldenburg. AWI conducts research activities to improve our understanding of the way polar regions function and their role in the global climate system. This internship was carried out in the Climate Dynamics section. Led by Prof. Dr. Thomas Jung, this section focuses on climate prediction and analysis of data from polar regions to obtain information on their dynamics and their impact on global climate dynamics. The section strives to understand the complex interactions between the different earth components which are the atmosphere, the ocean, and the cryosphere. Since its creation in 1980, the AWI has commissioned numerous field campaigns. It even benefits from its own icebreaker, the Polarstern, with which teams from all disciplines embark towards the polar regions in order to collect valuable data and advance polar research. These campaigns are places of strong international exchanges which reflect the institute’s commitment to international cooperation in research. The AWI brings together more than 1000 employees divided into some 20 sections, each specializing in different aspects of polar sciences. (Biology, Geosciences, and Climate Sciences). This interdisciplinarity forms a rich scientific community and allows effective collaboration to advance polar research.

4 Abstract

The closed geography of the Arctic Ocean makes it an ideal place for sea ice deformation. Unlike Antarctica, where sea ice can move freely, in the Arctic, the coastline restricts the ice in the basin, leading to collisions within the sea ice. As a result, leads and pressure ridges are dominant features of the Arctic sea ice cover. These features greatly affect the drag surface and heat fluxes at the air-ice-ocean interface. Because of their elongated shape, they are called

linear kinematic features (LKFs). In this paper, we seek to detect (and track) these LKFs following Hutter et al. (2019) algorithm. This algorithm is applied to the outputs of 7 simulations using different yield curves in the MITgcm, as well as to satellite observations. A comparison of the statistical distribution of 5 different metrics is made between the resolved LKFs of the 7 simulations and satellite data. The results highlight the strengths and weaknesses of each yield curve across all metrics, without being conclusive as to which yield curve significantly outperforms the others across all metrics. However, this work has made it possible to identify the points that still need to be worked on in order to better resolve the LKFs in the MITgcm.

5 Introduction

The Arctic Ocean is covered by a mosaic of sea ice floes, formed by continuous and omnipresent deformation that concentrates in narrow bands along floe boundaries, where the ice breaks and ridges in divergent, convergent, and shear motions. Recently, the focus of the sea ice modeling community on thermodynamics and large-scale circulation of sea ice has extended to resolving these small-scale deformation processes in sea ice dynamics. High-resolution applications as well as changes to the model physics describing the material properties of ice allow explicitly resolving deformation that is localized in narrow lines consisting of segments of leads and pressure ridges. These elongated deformation bands are referred to as Linear Kinematic Features (LKFs) (Kwok, 2001). Leads and pressure ridges represent only a small fraction of the large-scale ice cover, but their presence changes the interaction of sea ice with the ocean and atmosphere in the Arctic climate system substantially. The opening of the ice cover in a lead results in intensified heat and humidity exchange between the ocean and atmosphere, resulting in ice growth, brine rejection in the ocean, and convective processes in both the ocean and atmosphere. Sea ice piles up at pressure ridges, creating regional surface roughness. This roughness affects atmospheric and oceanic boundary layer circulation, snow distribution and drag forces acting on the ice (Martin et al., 2016). The objective of this study is to apply the detection (and tracking) algorithms described by Hutter et al. (2019) to simulation data with different rheologies. The rheology of sea ice corresponds to the deformation and flow characteristics of sea ice under the effect of applied stresses, such as wind or ocean currents. Thus, by varying rheology, we change the response of sea ice to these stresses, and we can obtain ice characteristics that differ greatly from one rheology to another, including aspects such as geographical distribution or thickness. Specifically, we aim to investigate whether changes in rheology have a discernible impact on the way the model simulates LKFs, as determined through statistical analysis. The characteristics of simulated LKFs are then compared with the characteristics of LKFs detected from RGPS data, allowing for a comprehensive evaluation of the model’s performance under different rheological scenarios.

6 Method

The aim of this study is therefore to compare the statistics of LKFs detected from different simulations with the statistics of LKFs detected from satellite observations. For this we used a set of LKFs detected by Hutter et al. (2019) from satellite observations, outputs from 7 different simulations and algorithms for detecting and tracking LKFs. We propose here to present these 3 tools:

6.1 RGPS

The satellite observation data used in this study are derived from the RADARSAT Geophysical Processor System (RGPS), which tracks ice motion in SAR images. Here we used the LKFs detected and tracked by Hutter et al. (2019). These LKFs were obtained from a RGPS Lagrangian deformation composite dataset which is constructed using the weighted-average pre-processing method described in Bouchat and Tremblay (2020) and Hutter and Losch (2020). The Lagrangian deformation data was obtained from Lagrangian drift data corresponding to satellite observations. These satellite observations consist of the placement of virtual buoys at the start of each winter. By tracking the drift of these buoys over time, they obtained a Lagrangian drift data set (Kwok, 1998). The position of the buoys is updated on average every 3 days, and the deformation calculated from these drifts is interpolated onto a regular grid with a spacing of 12.5 km. From this RGPS deformation data set, Hutter et al. (2019) generated a LKF (Linear Kinematic Features) data set for the winter (January-February-March) of 2008.

6.2 Simulations

The simulation data in this study are generated with a regional configuration of the Arctic using the Massachusetts Institute of Technology General Circulation Model (Marshall et al., 1997). The resolution is 4.5 km. The sea ice model (Losch et al., 2010) is based on a visco-plastic (VP) rheology. It is a dynamic and thermodynamic interactive sea ice model that allows easy activation and deactivation of various options, including the yield curves we'll be using in this study. Further details about this model can be found online (<https://mitgcm.org>). Since sea ice exhibits horizontal scales (from small floes of a few meters to larger-scale structures of several thousand kilometers) much greater than vertical scales (typically up to about ten meters at compression ridges), it is represented in 2D in most models. In our case, the model solves the vertically integrated 2D sea ice momentum equation:

$$m \frac{\partial \mathbf{u}}{\partial t} = -mf\mathbf{k} \cdot \mathbf{u} + \tau_a + \tau_o - mg\nabla H + \nabla \cdot \sigma \quad (1)$$

where $m = \rho_i h$ is sea ice mass per grid cell area and h is the grid-cell averaged mean ice thickness. \mathbf{u} is the sea ice velocity, f is the Coriolis parameter, \mathbf{k} is the vertical unit vector, g is the gravitational acceleration, ∇H is the gradient of the

sea surface height, and σ is the (vertically integrated) stress tensor. It is the form of the σ tensor that gives sea ice its rheology, material properties. τ_a and τ_o are ice-atmosphere and ice-ocean interfacial stress, taking into account seawater and air densities, water drag coefficient, velocities of the surface wind and surface currents of the ocean; and the rotation matrices that act on wind/current vectors

In the VP model, the component σ_{ij} of the stress tensor σ in (1) is a function of deformation sea ice strain rate $\dot{\epsilon}_{ij}(i, j = 1, 2)$ and sea ice strength P , bulk viscosity ζ and shear viscosity η (Hibler, 1979):

$$\sigma_{ij} = 2\eta\dot{\epsilon}_{ij} + (\zeta - \eta)\dot{\epsilon}_{kk}\delta_{ij} - \frac{P(1 - k_t)}{2}\delta_{ij} \quad (2)$$

with the strain rate $\dot{\epsilon}_{ij}(i, j = 1, 2)$ defined as:

$$\dot{\epsilon}_{ij} = \frac{1}{2}\left(\frac{\partial u_i}{\partial x_j} + \frac{\partial u_j}{\partial x_i}\right) \quad (3)$$

$$\dot{\epsilon}_{kk} = \dot{\epsilon}_{11} + \dot{\epsilon}_{22} \quad (4)$$

and P is the maximum compressive stress defined as a function of the compressive strength of 1m ice P^* , mean sea ice thickness h , and the sea ice concentration A :

$$P = P^* h e^{-C^*(1-A)} \quad (5)$$

where $C^* = 20$ is an empirical constant.

The stress tensor σ_{ij} is a way of representing the state of stress in a material. The principal stresses σ_1 and σ_2 are the eigenvalues of this tensor. Stress invariants, such as mean normal stress (σ_I) and maximum shear stress (σ_{II}), are quantities that remain unchanged regardless of the orientation of the coordinate system. They are often used to simplify stress analysis :

$$\sigma_I = \frac{1}{2}(\sigma_1 + \sigma_2) = \frac{1}{2}(\sigma_{11} + \sigma_{22}) \quad (6)$$

$$\sigma_{II} = \frac{1}{2}(\sigma_1 - \sigma_2) = \frac{1}{2}\sqrt{(\sigma_{11} - \sigma_{22})^2 + 4\sigma_{12}^2} \quad (7)$$

The expressions for bulk viscosity ζ and shear viscosity η depend on the yield curve used. The yield curve describes the threshold stress level at which sea ice begins to fail, to behave plastic deformation. This curve represents the point of transition from a viscous behavior, where there is a restoring force limiting sea ice to small deformations, to a plastic behavior, that allows large deformation events and limits the building of additional stress (Ringeyen, 2020). Thus, by varying the yield curve, we can modify the stress tensor and thereby obtain a very different behavior of sea ice from one yield curve to another. The objective here is to see how these changes in the yield curve, and thus in the stress tensor, impact the resolution of the LKFs. Since LKFs are areas of strong deformation, we expect these variations to have a significant impact on the resolution of these LKFs.

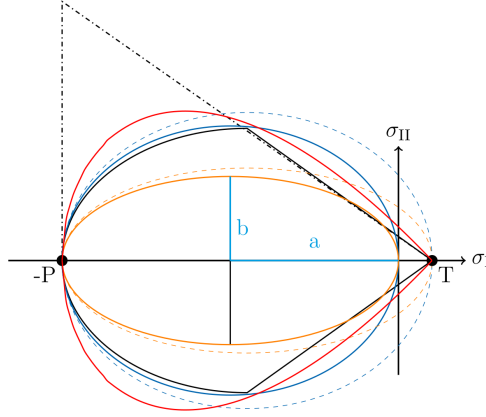


Figure 1: (from Liu (2023), adapted from Ringeisen et al. (2019)) : Schematic of the yield curves used in this study. Elliptical yield curve with ellipse aspect ratio $e = a/b = 2$ (orange, solid) and with tensile strength (orange, dashed); elliptical yield curve with ellipse aspect ratio $e = 1.25$ (blue, solid) and with tensile strength (blue, dashed); M.C.E. (black, dash-dotted) and T.E.M. (black, solid); Teardrop yield curve (red). P is the maximum compressive stress, T is the maximum tensile stress, σ_I represents the mean normal stress and σ_{II} the maximal shear stress

For this purpose, 7 simulations were conducted, each corresponding to a different yield curve:

6.2.1 Elliptical Yield Curve

The elliptical yield curve is the default yield curve in the MITgcm model, as well as the most commonly used yield curve in continuum sea-ice models. It is characterized by an elliptical shape. Bulk ζ and shear η viscosities :

$$\zeta_e = \frac{P(1 + k_t)}{2\Delta} \quad (8)$$

$$\eta_e = \frac{\zeta}{e^2} \quad (9)$$

are determined based on the aspect ratio of the ellipse $e = a/b$, which can be adjusted to represent different mechanical characteristics of sea ice. The ellipse aspect ratio e defines the shear strength S^* of the material as a fraction of its compressive strength P^* (Bouchat and Tremblay, 2017).

$$S^* = \frac{P^*(1 + k_t)}{e^2} \quad (10)$$

and T^* the tensile strength

$$T^* = k_t P^* \quad (11)$$

with k_t a tensile strength factor hence

$$S^* = (P^* + T^*) \frac{1}{e^2} \quad (12)$$

A low ratio e corresponds to a wider ellipse, therefore a higher maximal shear stress (σ_{II}) in the ice and a higher shear strength S^* . Conversely, a larger ratio e corresponds to a flatter ellipse indicating a relatively higher mean normal stress (σ_I) and a lower shear strength S^* . In our case, two ellipse ratios were used: a first $e = 2$ (less shear strength) and a second $e = 1.25$ (with more shear strength). Furthermore, in order to study its effect on the resolution of LKF in sea ice, a tensile factor k_t of 0.05 was added to the two ellipses mentioned above.

6.2.2 Mohr-Coulomb with elliptical plastic potential (M.C.E.):

The M.C.E. combines the characteristics of the Mohr-Coulomb curve and an elliptical flow rule. This allows pure shear deformations along its linear members (dash-dotted black straight lines in figure 1) to which is added the elliptical flow rule on the members (Ringeisen, 2020). Thus, it does not follow the normal flow rule :

$$\frac{\partial F}{\partial \sigma_{ij}} = \dot{\varepsilon}_{ij} \quad (13)$$

Which means that the strain rate and stress are not linearly proportional but follow an elliptical relationship. The bulk ζ and shear η viscosities of the M.C.E. :

$$\zeta_{MCE} = \frac{P(1 + k_t)}{2\Delta} \quad (14)$$

$$\eta_{MCE} = \frac{[\mu \frac{P(1-k_t)}{2\Delta} - \zeta\Delta + Pk_t]}{2} \dot{\varepsilon}_{II} \quad (15)$$

are determined as a function of the slope $\mu (= 0.7)$ of the Mohr-Coulomb curve (right part of the dash-dotted black lines in figure 1) and a tensile factor k_t . Here, the tensile factor chosen is the same as for elliptical curves $k_t = 0.05$.

6.2.3 Generalized Truncated Ellipse Method (T.E.M.) :

T.E.M. combines a truncated elliptical plasticity curve with the Mohr-Coulomb curve. This yield curve incorporates biaxial tensile stresses with the same tensile factor as M.C.E., E_2 and $E_{1.5,T}$.

The shear viscosity

$$\eta_{TEM} = \min \left\{ \eta_e, \frac{1}{\dot{\varepsilon}_{II}} \left[\mu \left(\frac{P(1-k_t)}{2} - \zeta \cdot \dot{\varepsilon}_{kk} \right) - c \right] \right\} \quad (16)$$

Symbol	Definition	E_2	$E_{2,T}$	$E_{1.5}$	$E_{1.5,T}$	M.C.E.	Teardrop	T.E.M.
e	Ellipse ratio (a/b)	2	2	1.25	1.25	1.4	/	1.4
k_t	Tensile strength factor	0	0.05	0	0.05	0.05	0.025	0.05
μ	Slope parameter	/	/	/	/	0.7	/	0.7

Table 1: Model parameters for each simulation

is determined in part as a function of the slope $\mu(= 0.7)$ of the Mohr-Coulomb curve (solid black lines on the right side of the curve in figure 1). Unlike the M.C.E., the T.E.M. incorporates a truncated elliptical plasticity curve with the normal flow rule in the high compression domain. Thus, in the case of significant normal stresses, the normal flow rule applies, the strain rates become linearly proportional to the stresses. For the rest of the constraints, the elliptical flow rule applies.

6.2.4 Teardrop

The Teardrop yield curve is a smooth compromise between a Mohr-Coulomb and an elliptical yield curve. It allows biaxial traction and follows the normal flow rule (deformation speeds linearly proportional to stresses). Bulk ζ and shear η viscosities

$$\zeta_{TD} = \frac{x + 1/2}{2\dot{\epsilon}_I} P \quad (17)$$

$$\eta_{TD} = \frac{-(x - k_t)(1 + x)^{1/2}}{2\dot{\epsilon}_{II}} P \quad (18)$$

where

$$x = \frac{\sigma_I}{P} = \frac{-(6 - 3k_t - 2l^2) + 2l\sqrt{l^2 + 3(1 + k_t)}}{9} \quad (19)$$

with

$$l = \frac{\dot{\epsilon}_I}{\dot{\epsilon}_{II}} \quad (20)$$

are determined based on different parameters, including tensile factor $k_t(= 0.025)$ and strain rates $\dot{\epsilon}_I$ & $\dot{\epsilon}_{II}$. It has the larger shear strength over E_2 ($e = 2$) and was originally designed to represent the homogeneous behavior of sets of oriented ice lines, such as fractures in sea ice Zhang and Rothrock (2005).

The parameters used in this study are detailed in Table 1. There are two elliptical yield curves without tensile strength: E_2 with an ellipse ratio $e = 2$ and $E_{1.5}$ with $e = 1.25$, following the normal flow rule. Additionally, two elliptical yield curves with tensile strength, $E_{2,T}$ ($e = 2, T$) and $E_{1.5,T}$ ($e = 1.25, T$), are discussed. $E_{1.5}$ ($e = 1.25$) and $E_{1.5,T}$ ($e = 1.25, T$) exhibit greater shear strength compared to E_2 ($e = 2$) and $E_{2,T}$ ($e = 2, T$), respectively. The tensile strength applied to $E_{1.5,T}$ ($e = 1.25, T$) and $E_{2,T}$ ($e = 2, T$) is the same tensile strength as the one used in the M.C.E. and T.E.M. yield curves. T.E.M. allows for biaxial

tensile strength under the normal flow rule along the elliptical part of the yield curve (Hibler and Schulson, 2000, Zhang and Rothrock, 2005). Teardrop allows for biaxial tensile stress, follows the normal flow rule, and exhibits higher shear strength than E_2 ($e = 2$) (Zhang and Rothrock, 2005). These seven yield curves have been documented and described in the thesis of Liu (2023) and have been utilized in the study of kinetic energy dissipation in sea ice. Here, these same yield curves are applied to the analysis of LKF representation in the MITgcm.

To align the simulation outputs with observational data from the RADARSAT Geophysical Processor System (RGPS), daily averages over a 3-day periods were computed. Similarly, for comparison with RGPS data from Hutter et al. (2022), we have also detected LKFs for winter 2008 only. Additionally, a geographical mask corresponding to the satellite coverage area was applied to the simulation outputs each 3-days period to ensure consistency with the RGPS data set. In the case of intersection angles, lifetimes and average LKF lengths, it was verified that masking had no significant impact on the results (not shown). In order to have a larger number of LKFs to analyze, masking was not applied to these data. Moreover, the LKF detection and tracking algorithms presented below require deformation data as input. Sea ice deformation is not simulated directly by the model, so it must be calculated. To this end, zonal and meridional drift data are used to obtain the divergent and shear (as well as vorticity) components of the deformation, to finally compute the total deformation. Shear is an output variable of the model. However, given that we are averaging over 3-day periods, we estimate that the values of these outputs after averaging are equivalent to those computed as follows.

6.3 Detection Algorithm

The algorithm used is described in detail in Hutter et al. (2019) We propose here to give a brief presentation. The detection algorithm used in this study requires as input a 2D field of the total deformation rate in the ice and provides as output a list of LKFs detected in this field. It was therefore necessary to compute the total deformation rate in the sea ice for each day, using the daily velocity data from the simulations presented above. The deformation rate from zonal and meridional velocities (U and V respectively) is calculated as follows:

$$\dot{\epsilon}_I = \frac{\partial U}{\partial x} + \frac{\partial V}{\partial y} \quad (21)$$

$$\dot{\epsilon}_{II} = \sqrt{\left(\frac{\partial U}{\partial x} - \frac{\partial V}{\partial y}\right)^2 + \left(\frac{\partial U}{\partial y} + \frac{\partial V}{\partial x}\right)^2} \quad (22)$$

$$\dot{\epsilon}_{tot} = \sqrt{\dot{\epsilon}_I^2 + \dot{\epsilon}_{II}^2} \quad (23)$$

With $\dot{\epsilon}_I$ and $\dot{\epsilon}_{II}$ corresponding to divergent (negative in the direction of convergence (eg. pressure ridge) and positive in the direction of divergence (e.g. lead)) and shear stresses respectively. Once the total strain rate had been calculated,

an image of this rate covering our study area could be generated. In order to be able to compare these data with data from RGPS observations, it was necessary to reproduce the 3-day sampling interval. Thus, for each 3-day period, the algorithm received 3 total strain rate images, which it combined to provide 1 list of LKFs per 3-day period. Once the images have been supplied to the algorithm, it proceeds as follows:

6.3.1 Data Processing and Filtering

First, the deformation images are processed to highlight areas of high deformation. Indeed, LKFs are defined as areas of high strain concentration. A Difference of Gaussian (DoG) filter is used to flag the LKFs in each daily deformation field. The kernel size has been adjusted based on the resolution difference between our simulations ($\Delta x_{\text{MIT}_{\text{gcm}}} = 4.5 \text{ km}$) and RGPS data ($\Delta x_{\text{RGPS}} = 12.5 \text{ km}$) by a factor: $\text{corfac} = \frac{1}{2} + \frac{1}{2} * \frac{\Delta x_{\text{RGPS}}}{\Delta x_{\text{MIT}_{\text{gcm}}}}$. At this stage, Pixels are flagged as LKF if their deformation exceeds the neighborhood's average rate (within 62.5 km) by 0.01 day^{-1} . This threshold is determined to be fine enough to filter all LKFs, but it is also high enough to prevent false detection of noise in the deformation fields caused by the momentum equation's lower accuracy. Only then are the 3 images combined into a single binary map, in which a pixel is considered as LKF if it is marked as LKF in any of the 3 daily images.

6.3.2 Segment Detection

At this stage, the algorithm detects small segments of pixels that form pieces of LKFs. Starting from the morphologically thinned binary map, the algorithm recognizes pixels that form lines. Thinning ensures that pixels on the same segment actually belong to the same LKF. For each point, the algorithm looks for neighboring cells that could belong to the same LKF, and stops as soon as it reaches the end of a segment or the angle between the two segments is too large.

6.3.3 Reconnection

Once it has produced all these segments, the algorithm goes through a reconnection phase. The idea here is to combine all the segments belonging to the same LKF into a single, longer segment. To achieve this, the algorithm uses the probability of a segment belonging to a group of segments as a function of its distance, orientation and local deformation rate. It then reconnects the segments with the highest probability until no match is found. In this way, the algorithm provides a list of segments belonging to the same LKF for 3 given images. The choice of parameters for this algorithm is very important, as it reacts very non-linearly to parameter changes. So, in order to obtain results comparable to those obtained in Hutter et al. (2022) for RGPS observations, the same parameters as those used by Hutter et al. (2022) have been used in this study.

Parameter	Name	Symbol	Value	Unit
Max. radius of DoG	max_kernel	r_2	5^a	pixels
Min. radius of DoG	min_kernel	r_1	1^a	pixels
DoG filtering threshold	dog_thres	d_{LKF}	0.01	
Max. elliptical distance	dis_thres	D_0	$4^{a,b}$	pixels
Elliptical factor	ellp_fac	e	2^b	
Max. difference in orientation	angle_thres	O_0	35^b	$^\circ$
Max. difference in deformation	eps_thres	$\dot{\epsilon}_0$	1.25^b	day^{-1}
Min. length	lmin	l_{min}	3^b	pixels

Table 2: Parameter table : List of parameters used in the LKF detection algorithm. ^a : Parameters related to length scales and need to be scaled with the spatial resolution corrector factor. ^b : Parameters not specified in Hutter et al. (2022), correspond to those used for the RGPS dataset detection in Hutter et al. (2019).

An example including a total strain rate map and the corresponding detected LKFs is shown in figure 2.

6.4 Tracking Algorithm

Secondly, in order to obtain temporal information on LKFs, such as lifetimes or growth rates, it was necessary to apply an LKF tracking algorithm. The tracking algorithm is presented in Hutter et al. (2019). Based on a list of LKFs and drift data, the algorithm tracks LKFs over time, giving a list of LKFs present on each day (or 3-day period in our case), both that day and the following day.

Tracking requires understanding the drift formation between the two datasets, and a first estimate of the position of each feature is calculated by considering advection. The estimated positions are converted into floating-point indices from detection. In this method, a tracked feature in the second dataset must overlap at least partially with the first estimate after considering growth and shrinkage. A search window is defined around the first estimate to check for feature overlap. The search window consists of pixels with rounded floating-point indices obtained from the first estimate. Features with a minimum number of pixels in the search window are marked as potentially tracked features. However, over the course of 3 days, features can grow or close, resulting in branching. The algorithm focuses on tracking growing and shrinking branches, as branching is complex to track. Therefore, a tracked feature may grow or shrink compared to the first dataset or only represent a part of the original feature.

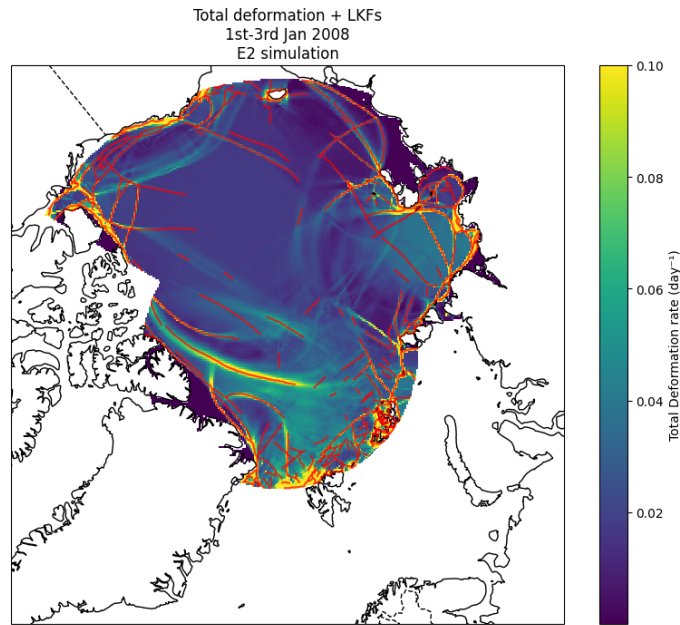


Figure 2: Map of the Arctic Basin with the total sea ice deformation rate as represented in the E_2 simulation for the days January 1-3, 2008. Above this deformation rate are shown in red the LKFs detected by the algorithm for the same day from this image.

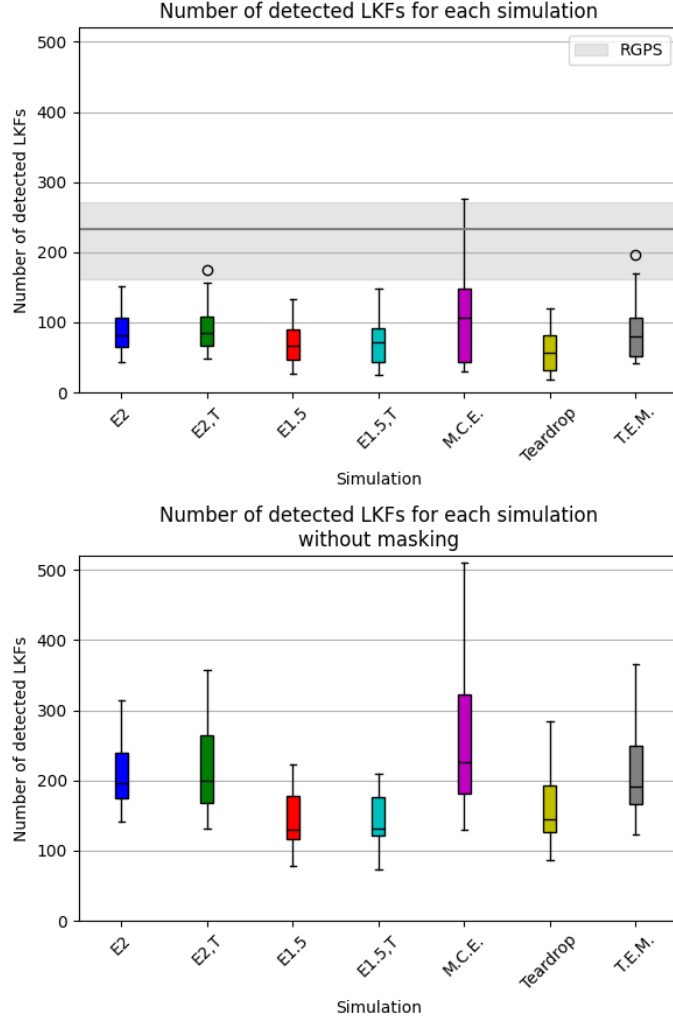


Figure 3: Boxplot of the number of detected linear kinematic features (LKFs) in 3-day intervals in all simulations masked over the RGPS observed area (upper panel) and over the Arctic Basin (lower panel). The range (over the studied period) of the number of LKF for each simulation is shown as a thin vertical line around the standard-deviation (colored boxes) and the median is represented as a black horizontal line. The black circles above the interval lines represent individual extreme values (outliers). The dark gray line represents the RADARSAT Geophysical Processor System mean value for reference and the shaded area the variability over 3 months (Jan-Feb-Mar).

7 Results

7.1 Number of LKFs

The analysis of the number of detected LKFs reveals that simulations generally show fewer LKFs per day compared to observations. This discrepancy can be attributed to the resolution dependency of the model. According to Hutter et al. (2022), the number of detected LKFs is proportional to the total number of grid cells associated with these features. For an LKF to be resolved in the model, it must be at least 9 km long (4.5 km per cell), as features confined to a single cell are not explicitly resolved. Therefore, only LKFs spanning two or more cells are resolved. With greater resolution achieved as the number of resolved LKFs increases. This partly explains why simulations detect fewer LKFs per day than observations; LKFs shorter than ten kilometers are not represented in the model.

Among the different simulations, notable differences in the average number of detected LKFs per day were observed. With over 100 LKFs (108), the M.C.E. simulation shows a wider spread and median closer to the RGPS mean, indicating a higher number of detected LKFs compared to other simulations. E2.T and T.E.M. have high medians (respectively 200 and 192 without mask and 85 and 80 with mask), but with more moderate variability compared to M.C.E. The fact that T.E.M. simulation shows results similar to both the $E_{2,T}$ and M.C.E. simulations is not surprising since the T.E.M. combines a truncated elliptical plasticity curve with the Mohr-Coulomb curve, balancing characteristics from both approaches. $E_{1.5}$ and $E_{1.5,T}$ have the lowest medians (~ 70 with the mask and ~ 130 without) and more restricted variability, indicating that they detect fewer LKFs more generally. E_2 and Teardrop have moderate medians (82 and 56 with the mask | 197 and 144 without) with reasonable variability. We note that for most simulations, masking does not change the relative number of LKFs, with M.C.E. still showing the most, followed by E2T, closely followed by E_2 and T.E.M. However, we note that Teardrop gains a lot of LKFs compared to the other simulations, so that while it shows the fewest LKFs with the mask, it shows more than $E_{1.5}$ and $E_{1.5,T}$ once the mask is removed. This suggests that many of the LKFs in the Teardrop simulation lie outside the boundaries of the zone observed by RGPS.

Comparing E_2 and $E_{2,T}$, we note that the addition of a tensile strength factor in $E_{2,T}$ results in a higher number of detected LKFs (median : 85 | 200) compared to E_2 (median : 82 | 197). Similarly, $E_{1.5,T}$, with a tensile strength factor, detects more LKFs (72 | 132) than $E_{1.5}$ (67 | 131). These comparisons seem to indicate that tensile strength factors enhance the resolution of LKFs.

Furthermore, the E_2 and $E_{2,T}$ simulations, which experience more compressive stress, detect more LKFs than the $E_{1.5}$ and $E_{1.5,T}$ simulations, which are subjected to more shear stress. This suggests that with more allowed shear stress ($e=1,25$), fewer failures occur, hence fewer LKFs.

The higher average number of LKFs and greater standard deviation in the M.C.E. simulation is somewhat surprising, given that the M.C.E. yield curve

is based on an elliptical plastic potential. These high values appear to be the result of noise in the M.C.E. simulation, as grid artifacts can be seen in the simulation, which could explain these surprisingly high values.

7.2 Length

7.2.1 Total length

The total length of LKFs is a critical metric as it reflects the potential surface area for air-ice-ocean interactions. Unlike the mere count of LKFs, the total length provides insights into the extent of these interactions. It is important to note that the total length of LKFs depends not only on the number of LKFs but also on their individual lengths, which will be discussed in the next subsection.

As observed on figure 4, the M.C.E. simulation has the longest total LKF length, nearly 14,000 km in the RGPS area and 52,000 km on the entire basin. This result aligns with expectations, as it is also the simulation with the highest number of LKFs. Conversely, the $E_{1.5}$, $E_{1.5,T}$ and Teardrop simulations, which have the shortest total length of LKFs at about 10,000 km in the RGPS area and 37,000 km in the entire Arctic, also have the lowest number of LKFs. The total lengths of LKFs in the other simulations (T.E.M. and the other 2 elliptical simulations, E_2 and $E_{2,T}$) appear to follow the number of resolved LKFs, suggesting that the average lengths per LKF are similar across different simulations. Overall the total lengths in these simulations are consistent with the number of LKFs detected, supporting the hypothesis that the average LKF lengths are comparable.

7.2.2 LKF length

The distribution of LKF lengths in the RADARSAT Geophysical Processor System (RGPS) dataset is heavy-tailed and can be described by a stretched exponential distribution (Hutter et al., 2019a). Here, in order to have more LKFs, RGPS data masking has not been applied to the simulation data. This distribution is shown in figure 5.

The average LKF lengths across different simulations are very similar (around 130 km when masked and 230 km unmasked), confirming the hypothesis that the lengths per LKF do not vary significantly between simulations. This consistency in LKF length explains why simulations with fewer LKFs also exhibit shorter total LKF lengths. The only exception is the M.C.E. simulation, which shows significantly shorter LKFs than the other simulations once masking is removed (195 km). This means that LKFs outside the masking zone are on average shorter than those in the zone. This observation may once again be due to the grid artifacts mentioned above, generating shorter 'false' LKFs. This explains why the total length of M.C.E. is 35% greater than the average of other simulations with masking, and only 22% greater without masking.

As shown in figure 5 it seems that simulations tend to overall overestimate the number of long LKFs and underestimate the number of short LKFs compared to the RGPS data. This phenomenon, noted by Hutter (2022), can be

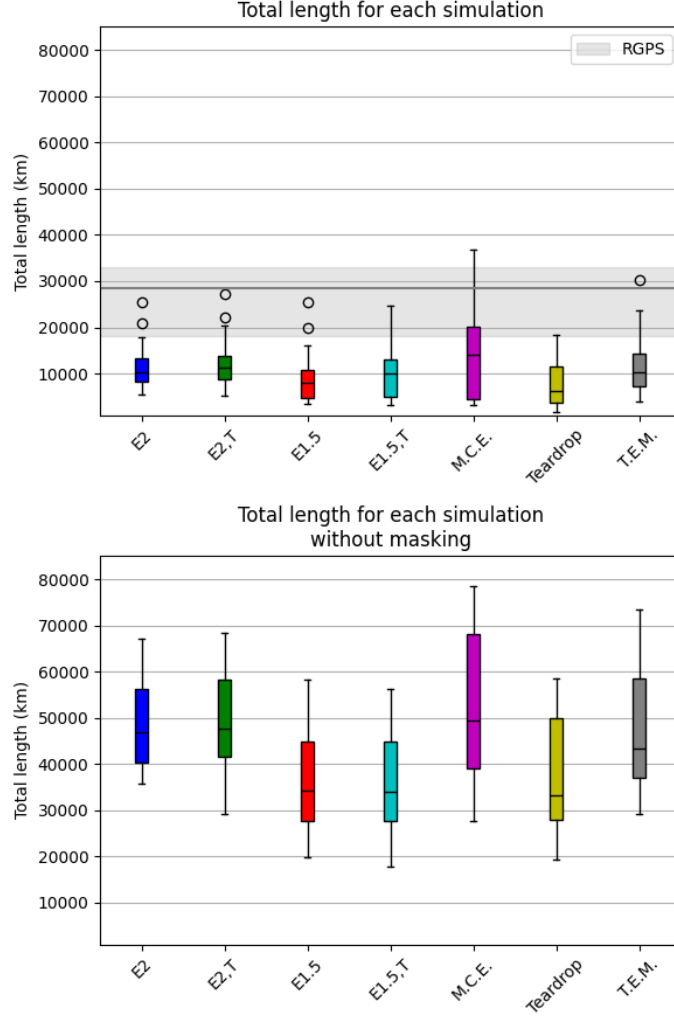


Figure 4: The total length of all LKFs together in 3-day intervals in all simulations masked over the RGPS observed area (upper panel) and over the Arctic Basin (lower panel). The range (over the studied period) of the total length of LKFs for each simulation is shown as a thin vertical line around the standard-deviation (colored boxes) and the median is represented as a black horizontal line. The black circles above the interval lines represent individual extreme values (outliers). The dark gray line represents the RADARSAT Geophysical Processor System mean value for reference and the shaded area the variability over 3 months (Jan-Feb-Mar).

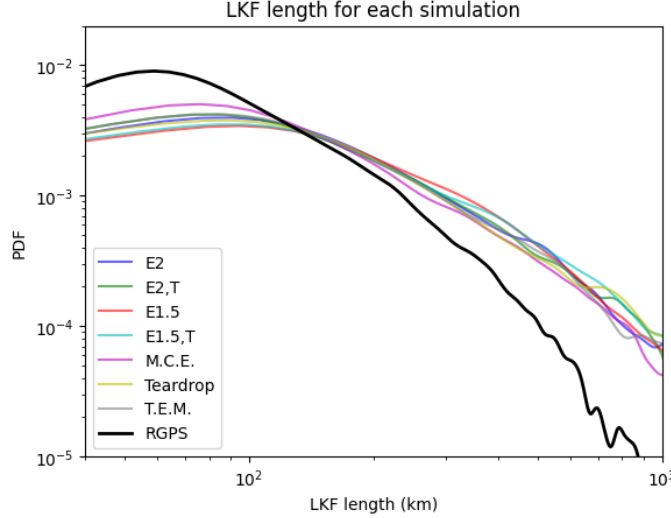


Figure 5: Distribution (probability distribution functions (PDFs)) of linear kinematic feature (LKF) lengths for all simulations and RADARSAT Geophysical Processor System (RGPS).

attributed to the lower number of LKFs detected in simulations relative to observations. Indeed, in areas with a higher density of LKFs, the chances of LKF intersecting with another increase, resulting in shorter individual LKFs. Conversely, in simulations with fewer LKFs, there are fewer intersection opportunities, allowing LKFs to reach greater lengths.

The similarity in average LKF lengths across the 7 different simulations indicates a uniform resolution of LKFs, irrespective of the simulation's rheology. The tendency of simulations to overestimate the number of long LKFs while underestimating shorter ones suggests a LKF's resolution limit inherent to the model's resolution. The total length of LKFs in simulations is heavily influenced by the number of LKFs detected, with fewer LKFs leading to longer individual lengths due to reduced intersection opportunities.

7.3 Intersection Angle

The observational data from both satellite imagery and laboratory measurement show a notable peak between 40° and 60° (Cunningham et al., 1994, Schulson and Hibler, 2004, Walter and Overland, 1993, Wang, 2007, Schulson et al., 2006) that the models fail to reproduce accurately. This peak has been described as being the result of sea ice following a Mohr behavior (Erlingsson, 1988). Consequently, Mohr-Coulomb and T.E.M. yield curves, both of which are designed to model granular materials with a Mohr-Coulomb behavior are expected to perform better in approximating this peak.

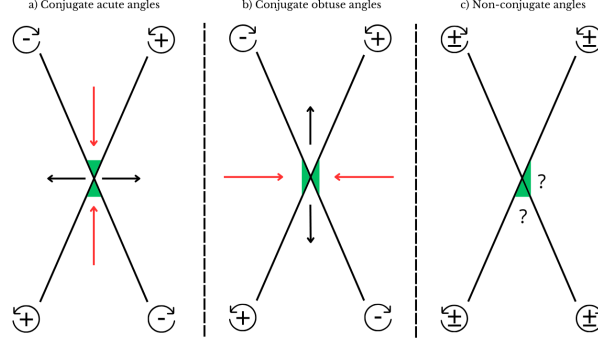


Figure 6: Schematic of intersection angle calculation for conjugate faults (panels a and b) and non-conjugate faults (panel c). For conjugate faults, the angle selected is the one with the greatest compressive strength (red arrows). For non-conjugate faults, both possible angles are selected.

To get closer to this 45° peak, we've focused here on the angles formed by conjugate faults. Conjugate faults correspond to 2 faults that form under the same compressive stress. For each pair of intersecting LKFs, 2 angles are possible, one acute and the other obtuse, their sum being 180° . For conjugate faults, the angle to be taken into account is measured in relation to the compressive stress. However, the direction of stress is not directly known from our simulation data. Thus, we follow the reasoning presented in Hutter et al. (2022) (also applied in Ringeisen et al. (2023)).

First, both segments are smoothed by applying a polynomial fitting (`poly_fit`) to smooth out random direction changes. Then the slope of each segment was computed and compared with another to determine the two possible angles. In order to decide which angle to be taken into account, we use the vorticity. As shown in figure 6, two conjugate faults have opposite vorticity signs. So, following the reasoning presented in figure 6 we can find the direction of compression and the corresponding angle. In the case of two identical vorticities, it is impossible to establish a clear constraint, so both angles are taken into account, each weighted by a factor of 0.5. In order to have a larger number of LKFs for computing intersection angles, the simulation data are not masked by the geographical area covered by the observations.. In this way, the statistics obtained are more robust. The results are shown figure 7.

All elliptical simulations are close to observations for estimating angles between 0° and 20° . From 20° to 90° , the E_2 and $E_{2,T}$ simulations tend to underestimate the angles, then overestimate them between 80° - 90° and beyond. By

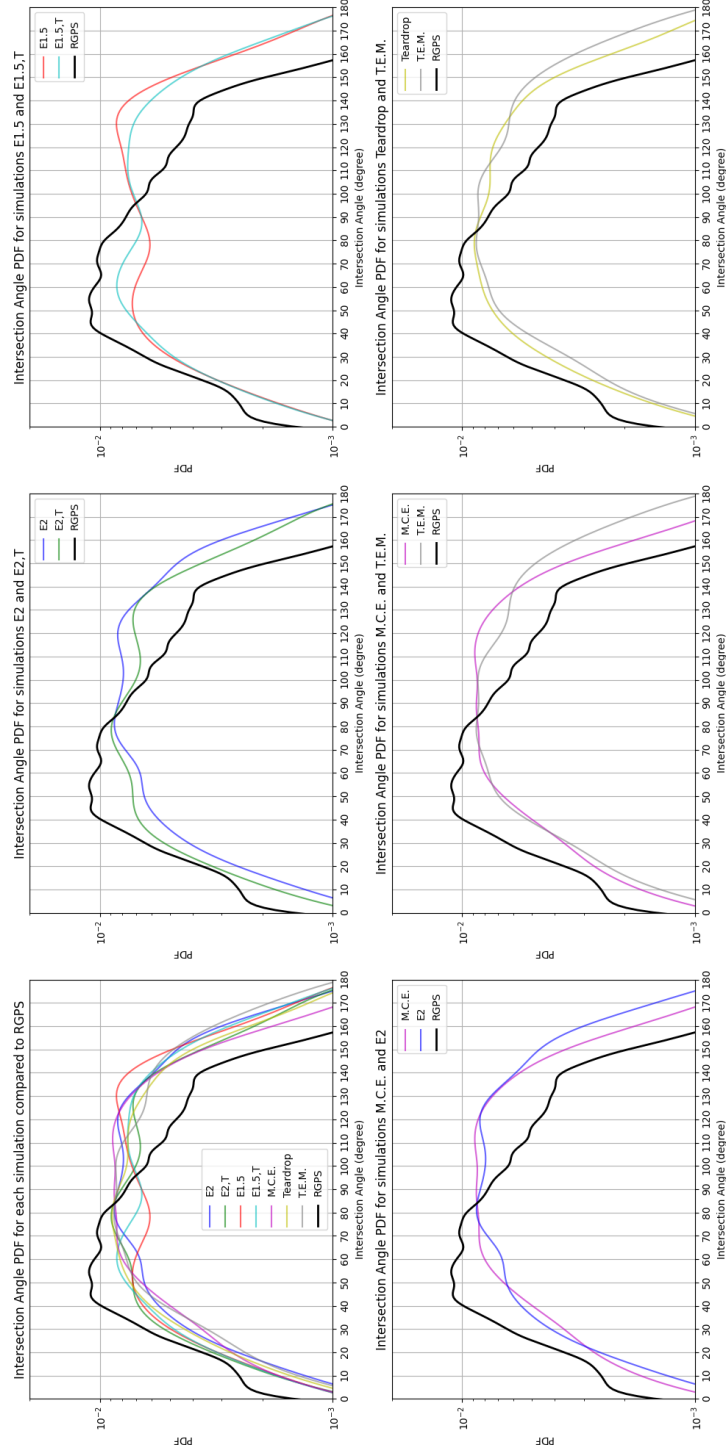


Figure 7: Distributions (probability distribution functions (PDFs)) of intersection angles between pairs of linear kinematic features for RADARSAT Geophysical Processor System (RGPS) and all simulations.

contrast, $E_{1.5}$ and $E_{1.5,T}$ better represent angles from 0 to 60°, even peaking at 50° as hoped. However, they greatly overestimate obtuse angles, showing a second peak around 130° (complementary angle to the first peak $180-50 = 130$). The M.C.E. simulation shows a similar behavior to E_2 , with a strong underestimation of acute angles under 70° and a strong overestimation of obtuse angles. It also seems to peak around 90°. This peak at 90° is thought to be the consequence of numerical noise. Indeed, as previously mentioned, the M.C.E. simulation is noisy and shows perpendicular lines on its total deformation 2D field (not shown). Thus this peak at 90° certainly corresponds to these grid artifacts. The T.E.M. simulation, on the other hand, is very close to the M.C.E. simulation but is more in line with our expectations, with less overestimation of obtuse angles above 120°. However, T.E.M. shows a right-shifted peak around 90° (not present in the observations) and still a significant overestimation of obtuse angles. Finally, the Teardrop simulation seems to be the closest to the observations, with a peak between 40-60° as seen so far only in the observations. However, this peak is wider than in the observations and extends up to $\sim 90^\circ$, which the observations don't do, followed by a second, weaker peak around 120°. Despite these inconsistencies with the observations, Teardrop still seems to be the best compromise, since it overestimates obtuse angles less than the elliptical simulations and presents the peak (starting at 40°) closest to that described by the observations among the 3 other simulations.

7.4 Lifetime

The lifetime of an LKF describes the period during which the LKF is actively deforming. The lifetime of LKFs and the area covered by LKFs are key factors in air-ice-ocean interaction. For example, heat exchange at the leads is highly dependent on its opening duration. Hutter et al. (2019) found that the distribution of lifetimes shows an exponential tail with the majority of LKF active the first three days with a rate parameter of 0.34 day^{-1} . Our results shown in figure 8 are in agreement with this article. Indeed, we observe an exponential decay of lifetimes as they increase with a rate parameter of around 0.40 day^{-1} (for RGPS data). With the majority of lifetimes less than or equal to 3 days, after 3 days we observe a drop in the number of LKFs still active.

As for the intersection angles after checking that this had no significant impact on the results, the data from simulations were not geographically masked here, in order to have more LKFs to analyze.

We note that all the simulations overestimate the number of older LKFs and thus overestimate the lifetime. Indeed, while for both simulations and observations, the majority of LKFs are less than 3 days old, with a mean rate parameter of 0.14 day^{-1} , the lifetime decreases almost 3 times faster for observations than for simulation data.

Simulations tend to overestimate the lifetime of LKFs, as observed by Hutter et al. (2022). Visco-plastic (VP) models, such as the MITgcm used here, show more inertia than in reality (M. Losch, personal communication, 2024-06-19). But also because in VP models, the strong localized deformation in the LKFs

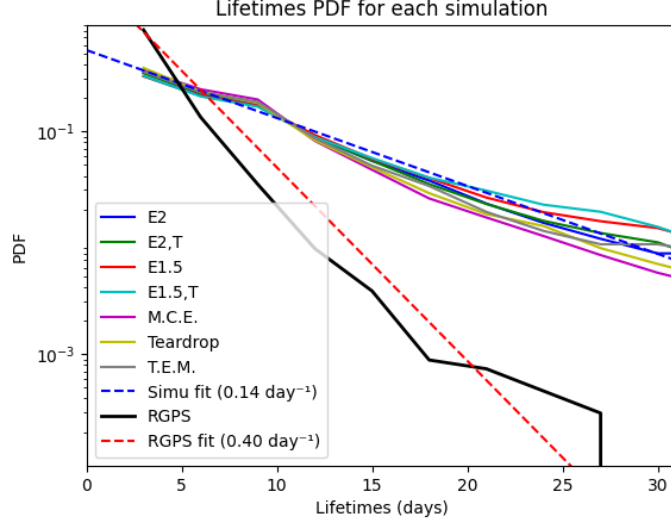


Figure 8: Distribution (probability distribution functions (PDFs)) of Linear kinematic feature lifetimes for RADARSAT Geophysical Processor System (RGPS) and all simulations. The dashed lines represent the exponential fits for both RGPS (red) and simulations (blue) data

reduces the concentration and thickness of the ice in these zones, which decreases the ice’s resistance. This reduction in resistance allows the deformation to concentrate and maintain itself in the LKFs, prolonging their lifespan. This feedback mechanism is not as pronounced in the real world, where other factors can rapidly destroy or disrupt LKFs. Furthermore, in simulations, past deformation events leave an imprint on the ice thickness distribution in a grid cell, influencing ice strength. This memory of deformation favours the continuation of deformation in the same zones, thus prolonging the life of LKFs (Hutter and Losch, 2020).

8 Outlook / Conclusion

In conclusion, elliptical yield curves perform overall less well than the others, with numbers and lengths particularly far from observations. Nevertheless, the addition of a tensile strength factor ($E_{2,T}$ and $E_{1.5,T}$) improves results for all the metrics analyzed in this study. In addition, decreasing the ellipse aspect ratio ($E_{1.5}$ and $E_{1.5,T}$) seems to improve intersection angles, but leads to a deterioration in results in terms of numbers and lengths, with results further from observations (compared with E_2 and $E_{2,T}$). The Teardrop yield curve looks very promising, as it offers a slight improvement in the representation of intersection angles compared with other yield curves. However, it solves too

few LKFs. In this sense, the T.E.M. yield curve seems to perform better, as it presents similar results in terms of intersection angles, but manages to solve more LKFs. Finally, the M.C.E. yield curve seems to perform better than the other yield curves outside the intersection angles, with numbers, lengths and lifetimes closer to the observations. However, these results cannot be significant due to the presence of numerical instability during simulation, which generates artifacts. Solving this instability problem would enable a better assessment of this yield curve, which looks promising. What remains to be resolved is the overestimation of lifetimes by all simulations, as well as the distribution of LKF lengths, which are relatively similar for all simulations and notably far from observations.

To pursue this study, it would be relevant to replicate it over a period of two full winters. This would enable us to capture the seasonal cycle and interannual variability in detail. In addition, it would be interesting to apply an approach similar to that of Hutter et al. (2022) using Maxwell Elastic Brittle (MEB) rheology (currently being implemented in the MITgcm) to observe the resolutions of Linear Kinematic Features (LKFs) with such a rheology.

Coupling with an atmospheric model could also enrich our understanding. However, given that LKFs are relatively small structures (a few hundred km in length at most), this would require the use of a high-resolution atmospheric model. Conventional atmospheric models generally operate at resolutions of the order of hundreds of kilometers, due to the high Reynolds number in the atmosphere. Thus, the use of a regional model may be more appropriate in this context.

As for coupling with an ocean model, these often benefit from higher resolutions than atmospheric models and could therefore better resolve LKFs. However, the impact of LKFs on the underlying ocean could be limited due to the strong halocline in the Arctic, which restricts heat fluxes. Indeed, the halocline acts as a barrier that limits these exchanges by restricting the upwelling of warm water from deeper layers to the surface. In other words, it limits the amount of heat that can be transported from the ocean to the atmosphere through these openings.

9 Code availability

All the codes used for detection, tracking and statistical analysis in this study can be found on my github: https://github.com/evalmr/LKF_MITgcm

References

Amélie Bouchat and Bruno Tremblay. Using sea-ice deformation fields to constrain the mechanical strength parameters of geophysical sea ice. *Journal of Geophysical Research: Oceans*, 122(7):5802–5825, 2017. ISSN 2169-9291. doi: 10.1002/2017JC013020. URL <https://doi.org/10.1002/2017JC013020>.

- [//onlinelibrary.wiley.com/doi/abs/10.1002/2017JC013020](https://onlinelibrary.wiley.com/doi/abs/10.1002/2017JC013020). _eprint: <https://onlinelibrary.wiley.com/doi/pdf/10.1002/2017JC013020>.
- Amélie Bouchat and Bruno Tremblay. Reassessing the Quality of Sea-Ice Deformation Estimates Derived From the RADARSAT Geophysical Processor System and Its Impact on the Spatiotemporal Scaling Statistics. *Journal of Geophysical Research: Oceans*, 125(8):e2019JC015944, 2020. ISSN 2169-9291. doi: 10.1029/2019JC015944. URL <https://onlinelibrary.wiley.com/doi/abs/10.1029/2019JC015944>. _eprint: <https://onlinelibrary.wiley.com/doi/pdf/10.1029/2019JC015944>.
- G.F. Cunningham, R. Kwok, and J. Banfield. Ice lead orientation characteristics in the winter Beaufort Sea. In *Proceedings of IGARSS '94 - 1994 IEEE International Geoscience and Remote Sensing Symposium*, volume 3, pages 1747–1749, Pasadena, CA, USA, 1994. IEEE. ISBN 978-0-7803-1497-9. doi: 10.1109/IGARSS.1994.399553. URL <http://ieeexplore.ieee.org/document/399553/>.
- Björn Erlingsson. Two-Dimensional Deformation Patterns in Sea Ice. *Journal of Glaciology*, 34(118):301–308, January 1988. ISSN 0022-1430, 1727-5652. doi: 10.3189/S0022143000007061. URL <https://www.cambridge.org/core/journals/journal-of-glaciology/article/twodimensional-deformation-patterns-in-sea-ice/61488676352882C4B54A785AF642B048>.
- W. D. Hibler. A Dynamic Thermodynamic Sea Ice Model. July 1979. ISSN 1520-0485. URL https://journals.ametsoc.org/view/journals/phoc/9/4/1520-0485_1979_009_0815_adtsim_2_0_co_2.xml. Section: Journal of Physical Oceanography.
- W. D. Hibler and Erland M. Schulson. On modeling the anisotropic failure and flow of flawed sea ice. *Journal of Geophysical Research: Oceans*, 105(C7):17105–17120, 2000. ISSN 2156-2202. doi: 10.1029/2000JC900045. URL <https://onlinelibrary.wiley.com/doi/abs/10.1029/2000JC900045>. _eprint: <https://onlinelibrary.wiley.com/doi/pdf/10.1029/2000JC900045>.
- Nils Hutter and Martin Losch. Feature-based comparison of sea ice deformation in lead-permitting sea ice simulations. *The Cryosphere*, 14(1):93–113, January 2020. ISSN 1994-0416. doi: 10.5194/tc-14-93-2020. URL <https://tc.copernicus.org/articles/14/93/2020/>. Publisher: Copernicus GmbH.
- Nils Hutter, Lorenzo Zampieri, and Martin Losch. Leads and ridges in Arctic sea ice from RGPS data and a new tracking algorithm. *The Cryosphere*, 13(2): 627–645, February 2019. ISSN 1994-0416. doi: 10.5194/tc-13-627-2019. URL <https://tc.copernicus.org/articles/13/627/2019/>. Publisher: Copernicus GmbH.

- Nils Hutter, Amélie Bouchat, Frédéric Dupont, Dmitry Dukhovskoy, Nikolay Koldunov, Younjoo J. Lee, Jean-François Lemieux, Camille Lique, Martin Losch, Wieslaw Maslowski, Paul G. Myers, Einar Ólason, Pierre Rampal, Till Rasmussen, Claude Talandier, Bruno Tremblay, and Qiang Wang. Sea Ice Rheology Experiment (SIREx): 2. Evaluating Linear Kinematic Features in High-Resolution Sea Ice Simulations. *Journal of Geophysical Research: Oceans*, 127(4):e2021JC017666, 2022. ISSN 2169-9291. doi: 10.1029/2021JC017666. URL <https://onlinelibrary.wiley.com/doi/abs/10.1029/2021JC017666>. eprint: <https://onlinelibrary.wiley.com/doi/pdf/10.1029/2021JC017666>.
- R. Kwok. The RADARSAT Geophysical Processor System. In Costas Tsatsoulis and Ronald Kwok, editors, *Analysis of SAR Data of the Polar Oceans: Recent Advances*, pages 235–257. Springer, Berlin, Heidelberg, 1998. ISBN 978-3-642-60282-5. doi: 10.1007/978-3-642-60282-5_11. URL https://doi.org/10.1007/978-3-642-60282-5_11.
- Ronald Kwok. Deformation of the Arctic Ocean Sea Ice Cover between November 1996 and April 1997: A Qualitative Survey. In J. P. Dempsey and H. H. Shen, editors, *IUTAM Symposium on Scaling Laws in Ice Mechanics and Ice Dynamics*, pages 315–322, Dordrecht, 2001. Springer Netherlands. ISBN 978-94-015-9735-7. doi: 10.1007/978-94-015-9735-7_26.
- Yuqing Liu. Landfast ice in the Arctic: parameterization in numerical modeling and effects on the hydrography. March 2023. doi: 10.26092/elib/2100. URL <https://media.suub.uni-bremen.de/handle/elib/6761>. Accepted: 2023-03-24T10:26:58Z Publisher: Universität Bremen.
- Martin Losch, Dimitris Menemenlis, Jean-Michel Campin, Patick Heimbach, and Chris Hill. On the formulation of sea-ice models. Part 1: Effects of different solver implementations and parameterizations. *Ocean Modelling*, 33(1):129–144, January 2010. ISSN 1463-5003. doi: 10.1016/j.ocemod.2009.12.008. URL <https://www.sciencedirect.com/science/article/pii/S1463500309002418>.
- John Marshall, Alistair Adcroft, Chris Hill, Lev Perelman, and Curt Heisey. A finite-volume, incompressible Navier Stokes model for studies of the ocean on parallel computers. *Journal of Geophysical Research: Oceans*, 102(C3):5753–5766, 1997. ISSN 2156-2202. doi: 10.1029/96JC02775. URL <https://onlinelibrary.wiley.com/doi/abs/10.1029/96JC02775>. eprint: <https://onlinelibrary.wiley.com/doi/pdf/10.1029/96JC02775>.
- Torge Martin, Michel Tsamados, David Schroeder, and Daniel L. Feltham. The impact of variable sea ice roughness on changes in Arctic Ocean surface stress: A model study. *Journal of Geophysical Research: Oceans*, 121(3):1931–1952, 2016. ISSN 2169-9291. doi: 10.1002/2015JC011186. URL <https://onlinelibrary.wiley.com/doi/abs/10.1002/2015JC011186>. eprint: <https://onlinelibrary.wiley.com/doi/pdf/10.1002/2015JC011186>.

- Damien Ringeisen. *Fracture Angles in Numerical Simulations of Sea Ice with Viscous-Plastic Rheologies*. PhD Thesis, Universität Bremen, 2020. URL <https://scholar.archive.org/work/xuastx2vtnhmdn4rqddtpmecxe/access/wayback/https://media.suub.uni-bremen.de/bitstream/elib/4583/1/thesis.pdf>.
- Damien Ringeisen, Martin Losch, L. Bruno Tremblay, and Nils Hutter. Simulating intersection angles between conjugate faults in sea ice with different viscous-plastic rheologies. *The Cryosphere*, 13(4):1167–1186, April 2019. ISSN 1994-0416. doi: 10.5194/tc-13-1167-2019. URL <https://tc.copernicus.org/articles/13/1167/2019/>. Publisher: Copernicus GmbH.
- Damien Ringeisen, Nils Hutter, and Luisa von Albedyll. Deformation lines in Arctic sea ice: intersection angle distribution and mechanical properties. *The Cryosphere*, 17(9):4047–4061, September 2023. ISSN 1994-0416. doi: 10.5194/tc-17-4047-2023. URL <https://tc.copernicus.org/articles/17/4047/2023/>. Publisher: Copernicus GmbH.
- E. M. Schulson, A. L. Fortt, D. Iliescu, and C. E. Renshaw. On the role of frictional sliding in the compressive fracture of ice and granite: Terminal vs. post-terminal failure. *Acta Materialia*, 54(15):3923–3932, September 2006. ISSN 1359-6454. doi: 10.1016/j.actamat.2006.04.024. URL <https://www.sciencedirect.com/science/article/pii/S1359645406003120>.
- Erland M. Schulson and William D. Hibler. Fracture of the winter sea ice cover on the Arctic ocean. *Comptes Rendus Physique*, 5(7):753–767, September 2004. ISSN 1631-0705. doi: 10.1016/j.crhy.2004.06.001. URL <https://www.sciencedirect.com/science/article/pii/S1631070504001318>.
- Bernard A. Walter and James E. Overland. The response of lead patterns in the Beaufort Sea to storm-scale wind forcing. *Annals of Glaciology*, 17:219–226, January 1993. ISSN 0260-3055, 1727-5644. doi: 10.3189/S0260305500012878. URL <https://www.cambridge.org/core/journals/annals-of-glaciology/article/response-of-lead-patterns-in-the-beaufort-sea-to-stormscale-wind-forcing/43BF1A611FEAF0F5EA4DFFAA9236F11F>.
- Keguang Wang. Observing the yield curve of compacted pack ice. *Journal of Geophysical Research: Oceans*, 112(C5), 2007. ISSN 2156-2202. doi: 10.1029/2006JC003610. URL <https://onlinelibrary.wiley.com/doi/abs/10.1029/2006JC003610>. eprint: <https://onlinelibrary.wiley.com/doi/pdf/10.1029/2006JC003610>.
- Jinlun Zhang and D. A. Rothrock. Effect of sea ice rheology in numerical investigations of climate. *Journal of Geophysical Research: Oceans*, 110(C8), 2005. ISSN 2156-2202. doi: 10.1029/2004JC002599. URL <https://onlinelibrary.wiley.com/doi/abs/10.1029/2004JC002599>. eprint: <https://onlinelibrary.wiley.com/doi/pdf/10.1029/2004JC002599>.